

RESEARCH BRIEF

Efficacy of a Small-Molecule Inhibitor of Kras^{G12D} in Immunocompetent Models of Pancreatic Cancer



Samantha B. Kemp^{1,2}, Noah Cheng^{1,2}, Nune Markosyan^{1,2}, Rina Sor^{1,2}, Il-Kyu Kim^{1,2}, Jill Hallin³, Jason Shoush^{1,2}, Liz Quinones^{1,2}, Natalie V. Brown^{1,2}, Jared B. Bassett^{1,2}, Nikhil Joshi^{1,2}, Salina Yuan^{1,2}, Molly Smith^{1,2}, William P. Vostrejs^{1,2}, Kia Z. Perez-Vale^{1,2}, Benjamin Kahn^{1,2}, Feiyan Mo^{1,2}, Timothy R. Donahue⁴, Caius G. Radu⁴, Cynthia Clendenin^{1,2}, James G. Christensen³, Robert H. Vonderheide^{1,2,5}, and Ben Z. Stanger^{1,2}

ABSTRACT

Mutations in the KRAS oncogene are found in more than 90% of patients with pancreatic ductal adenocarcinoma (PDAC), with Gly-to-Asp mutations (KRAS^{G12D}) being the most common. Here, we tested the efficacy of a small-molecule KRAS^{G12D} inhibitor, MRTX1133, in implantable and autochthonous PDAC models with an intact immune system. *In vitro* studies validated the specificity and potency of MRTX1133. *In vivo*, MRTX1133 prompted deep tumor regressions in all models tested, including complete or near-complete remissions after 14 days. Concomitant with tumor cell apoptosis and proliferative arrest, drug treatment led to marked shifts in the tumor microenvironment (TME), including changes in fibroblasts, matrix, and macrophages. T cells were necessary for MRTX1133's full antitumor effect, and T-cell depletion accelerated tumor regrowth after therapy. These results validate the specificity, potency, and efficacy of MRTX1133 in immunocompetent KRAS^{G12D}-mutant PDAC models, providing a rationale for clinical testing and a platform for further investigation of combination therapies.

SIGNIFICANCE: Pharmacologic inhibition of KRAS^{G12D} in pancreatic cancer models with an intact immune system stimulates specific, potent, and durable tumor regressions. In the absence of overt toxicity, these results suggest that this and similar inhibitors should be tested as potential, high-impact novel therapies for patients with PDAC.

See related commentary by Redding and Grabocka, p. 260.

INTRODUCTION

Pancreatic ductal adenocarcinoma (PDAC) is a lethal malignancy with a 5-year survival rate of only 11% (1). Although

advances in immunotherapy and targeted therapies have improved outcomes for many patients with cancer (2, 3), these benefits have not extended to PDAC, for which chemotherapy remains first-line treatment (4–6). As more than 90%

¹Department of Medicine, Perelman School of Medicine, University of Pennsylvania, Philadelphia, Pennsylvania. ²Abramson Cancer Center and Abramson Family Cancer Research Institute, Perelman School of Medicine, University of Pennsylvania, Philadelphia, Pennsylvania. ³Mirati Therapeutics, Inc., San Diego, California. ⁴Department of Molecular and Medical Pharmacology, University of California, Los Angeles, Los Angeles, California. ⁵Parker Institute for Cancer Immunotherapy, University of Pennsylvania, Philadelphia, Pennsylvania.

Corresponding Authors: Ben Z. Stanger, University of Pennsylvania Perelman School of Medicine, 421 Curie Boulevard, Philadelphia, PA 19104. Phone:

215-746-5560; E-mail: bstanger@upenn.edu; and Robert H. Vonderheide, University of Pennsylvania Perelman School of Medicine, 12 South Pavilion, 3400 Civic Center Boulevard, Philadelphia, PA 19104. Phone: 215-662-3929; E-mail: rhv@upenn.edu

Cancer Discov 2023;13:298–311

doi: 10.1158/2159-8290.CD-22-1066

This open access article is distributed under the Creative Commons Attribution-NonCommercial-NoDerivatives 4.0 International (CC BY-NC-ND 4.0) license.

©2022 The Authors; Published by the American Association for Cancer Research

of patients with PDAC harbor oncogenic mutations in the Kirsten Ras (*KRAS*) oncogene (7), the *KRAS* oncoprotein stands out as a particularly attractive target for novel PDAC therapy (8).

Prior studies using inducible genetic systems have shown that *KRAS* signaling has both cell-autonomous activity (e.g., effects on cell growth, proliferation, metabolism, and senescence) and non-cell-autonomous effects on the tumor microenvironment (TME; refs. 9–13). Although these features have made *KRAS* a prime target for anticancer therapy in PDAC and other malignancies, efforts to effectively block *KRAS* signaling have been challenging. Recently, several small-molecule inhibitors of mutant *KRAS* have been developed. To date, the most clinically advanced of these are drugs that target *KRAS*^{G12C}, leading to FDA approval(s) based on efficacy in a variety of solid tumors (14–18). However, *KRAS*^{G12C} mutations are present in only a small fraction of patients with cancer harboring *KRAS* mutations, and they are found in less than 1% of patients with PDAC (19). By contrast, *KRAS*^{G12D} mutations are present in ~40% of patients with PDAC (20), highlighting the importance of this mutant allele at a population level.

One feature that makes PDAC therapeutically challenging is the tumor's dense, immunosuppressive TME that includes immune cells, cancer-associated fibroblasts (CAF), and a dense extracellular matrix. The PDAC TME contributes to disease progression and is believed to limit the efficacy of therapeutic interventions (21). These features are recapitulated in a genetically engineered, autochthonous mouse model that incorporates mutant *Kras*^{G12D} and *Trp53*^{R172H} (KPC; ref. 22) and in which tumor cells can be identified with a YFP-lineage label (KPC/Y; ref. 23). Importantly, tumor-bearing KPC/Y mice are refractory to most therapeutic interventions (24), making this model useful for prioritizing therapeutic candidates and defining their mechanisms of action in an immunocompetent setting. In this study, we used the KPC/Y model, and several of its clonal derivatives, to test the efficacy and biological impact of MRTX1133, a novel inhibitor of *KRAS*^{G12D} (25, 26).

RESULTS

MRTX1133 Selectively Inhibits *KRAS*^{G12D} and Downstream MAPK Signaling *In Vitro*

To study the effect of *KRAS*^{G12D} inhibition on PDAC, we utilized MRTX1133, a small-molecule *KRAS*^{G12D} inhibitor. *In vitro*, MRTX1133 has a submicromolar half maximal inhibitory concentration (IC₅₀) across human (Supplementary Fig. S1A) and murine (Supplementary Fig. S1B) PDAC lines harboring *KRAS*^{G12D} mutations, consistent with prior reports (25, 26). By contrast, the BxPC-3 cell line, which harbors only wild-type *KRAS*, and the MIA PaCa-2 line, bearing mutant *KRAS*^{G12C}, were comparatively resistant, with an IC₅₀ in the micromolar range (Supplementary Fig. S1A). Similarly, non-PDAC cell lines bearing mutant *KRAS*^{G12C} [Lewis lung carcinoma (LLC); ref. 27] or wild-type *KRAS* (MC38; ref. 28) also exhibited sensitivity only in the micromolar range (Supplementary Fig. S1C). Using phosphorylated ERK1/2 (p-ERK1/2) as a downstream readout of *KRAS* activity, we observed a dose-dependent decrease in p-ERK1/2 levels in

both human (Supplementary Fig. S1D) and murine (Supplementary Fig. S1E) *KRAS*^{G12D}-mutant PDAC lines. To further assess how MRTX1133 affects downstream *KRAS* activity, we used phosphorylated AKT (p-AKT) and phosphorylated S6 (p-S6) as readouts for the PI3K/AKT/mTOR pathway. Unlike the dose-dependent decrease in p-ERK1/2, we did not detect any changes in p-AKT or p-S6 expression after MRTX1133 treatment, suggesting short-term treatment with MRTX1133 likely inhibits MAPK activity (Supplementary Fig. S1E).

Additionally, MRTX1133 treatment did not alter p-ERK1/2 levels in BxPC-3 human PDAC cells with wild-type *KRAS* (Supplementary Fig. S1F). Finally, we tested the efficacy of MRTX1133 in an isogenic murine PDAC cell line (4662; ref. 29) engineered to express *Kras*^{G12C} instead of *Kras*^{G12D}. As shown in Supplementary Fig. S1G, 4662-*Kras*^{G12C} cells were ~20-fold less sensitive to the drug *in vitro* compared with 4662-*Kras*^{G12D} cells. Taken together, these results demonstrate the selectivity of MRTX1133 for cells with mutant *Kras*^{G12D}.

Pharmacologic Inhibition of *KRAS*^{G12D} Inhibits Tumor Growth in Immunocompetent Implantation PDAC Models

We next assessed the activity of MRTX1133 *in vivo*. To evaluate MRTX1133 in an immune-competent setting, we implanted syngeneic 6419c5 PDAC cells into the flanks of C57BL/6 mice. 6419c5 is a clonal cell line derived from a C57BL/6-backcrossed KPC/Y tumor that gives rise to immunotherapy-resistant PDAC tumors containing YFP-labeled cancer cells (30). Once tumors reached a size of 20 to 80 mm³, we assigned mice to randomly receive either vehicle or MRTX1133 [30 mg/kg i.p. given twice a day (b.i.d.); refs. 25, 26]. Differences in tumor volume were evident as early as 2 days of MRTX1133 treatment (Fig. 1A), and after 7 days, 5 of 10 tumors (50%) exhibited regressions, whereas 5 of 10 (50%) exhibited modest or static tumor growth (Supplementary Fig. S2A). Concordantly, final tumor weights in the MRTX1133-treated group were significantly reduced compared with vehicle (Supplementary Fig. S2B).

To examine the specificity of MRTX1133 for *Kras*^{G12D} *in vivo*, we implanted the isogenic 4662-*Kras*^{G12C} and 4662-*Kras*^{G12D} cell lines (described above) into immune-competent animals and treated them with MRTX1133 or vehicle for 4 days. Consistent with our *in vitro* findings, tumors derived from 4662-*Kras*^{G12D} cells regressed, whereas those derived from 4662-*Kras*^{G12C} cells did not respond to the drug (Supplementary Fig. S2C). MRTX1133 treatment had no effect on the growth of LLC tumors harboring *Kras*^{G12C} mutations (ref. 27; Supplementary Fig. S2D) or on MC38 colon carcinoma tumors harboring wild-type *Kras* (ref. 28; Supplementary Fig. S2E). Thus, the selectivity of MRTX1133 activity for cells carrying *Kras*^{G12D} persists *in vivo*.

To further test the reproducibility of these effects, we used a third syngeneic *Kras*^{G12D} PDAC cell clone, 2838c3, which gives rise to T-cell-inflamed tumors that are responsive to combination immunotherapy (30). We subcutaneously implanted 2838c3 cells into immune-competent animals and randomized mice to either vehicle or MRTX1133 when tumors reached 20 to 80 mm³. After 7 days of MRTX1133 treatment, 8 of 8 (100%) tumors regressed (Fig. 1B; Supplementary

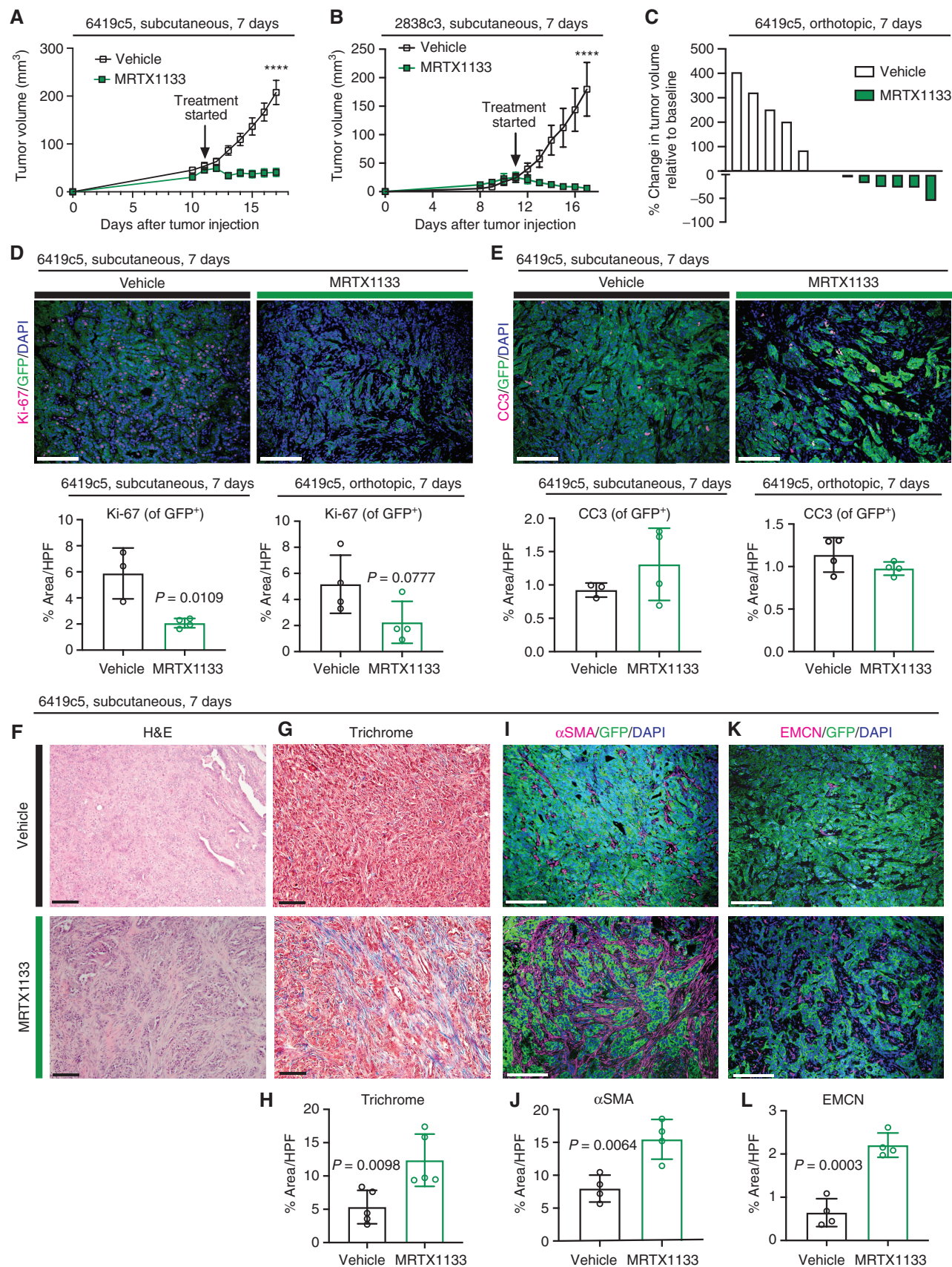


Fig. S2F). In contrast to 6419c5-derived tumors, 2 of 8 (25%) 2838c3-derived tumors had a complete remission (CR) after 7 days of treatment (Supplementary Fig. S2F). This difference in response was not due to variation in drug sensitivity, as 6419c5 cells are ~5-fold more sensitive to MRTX1133 than 2838c3 cells (Supplementary Fig. S1B).

The efficacy of antitumor agents can vary depending on the tumor site (31). To determine whether the effects of MRTX1133 are preserved in an orthotopic setting, we implanted 6419c5 cells into the pancreas of syngeneic hosts using ultrasound guidance (32). Mice were screened for tumor development by ultrasound and randomized to receive MRTX1133 or vehicle when tumors reached 20 to 80 mm³. After 7 days of therapy, regressions were seen in 6 of 6 (100%) tumors treated with MRTX1133 (Fig. 1C; Supplementary Fig. S2G and S2H). Despite these reductions in tumor size, none of the subcutaneously or orthotopically implanted 6419c5-derived tumors exhibited a CR. These results indicate that MRTX1133 has broad activity against multiple Kras^{G12D}-containing tumor lines, with the greatest efficacy observed in T cell-inflamed tumors that can undergo CR.

To explore the mechanism(s) driving the antitumor effect of MRTX1133, we stained vehicle- and MRTX1133-treated tumors for the proliferation marker Ki-67 and the apoptosis marker cleaved caspase-3 (CC3). Ki-67 staining, measured as a percentage of YFP⁺ tumor cells, was reduced in both subcutaneous and orthotopic tumors (Fig. 1D). By contrast, we did not detect a difference in CC3 staining after 7 days of MRTX1133 treatment in both subcutaneous and orthotopic tumors (Fig. 1E). Consistent with our *in vitro* findings, p-ERK1/2 staining was significantly reduced in both subcutaneous and orthotopic tumors treated with MRTX1133 (Supplementary Fig. S2I and S2J), whereas p-S6 expression was unaffected (Supplementary Fig. S2K). These results suggest that MRTX1133 manifests its effects by inhibiting cell proliferation, likely through a reduction in MAPK-ERK signaling.

Given the propensity of PDAC to metastasize, we next assessed the ability of MRTX1133 to reduce metastatic burden.

We injected 6419c5 cells via tail vein into C57BL/6 mice. PDAC cells were allowed to settle for 3 days before MRTX1133 treatment began. Mice were treated with vehicle or MRTX1133 for 7 days, and then we assessed the lungs for metastatic burden. MRTX1133 treatment resulted in a marked reduction in lung metastases as detected by YFP expression (Supplementary Fig. S3A–S3C). Further, MRTX1133-treated mice had a lower lung mass-to-body mass ratio, suggesting reduced metastatic burden (Supplementary Fig. S3D).

MRTX1133 Elicits Changes in the Tumor Stroma and Vasculature

The PDAC TME is composed of a dense fibrotic stroma (24, 33). Hematoxylin and eosin (H&E) staining performed after 7 days of MRTX1133 treatment revealed major changes in the TME (Fig. 1F), including an increase in collagen fibers as confirmed with Masson's trichrome (Fig. 1G and H). Given that myofibroblastic CAFs (myCAF) are a major source of collagen deposition in the TME (34), we quantified this population by staining for the myCAF marker alpha-smooth muscle actin (α SMA). This revealed a significant increase in α SMA⁺ fibroblasts in subcutaneous (Fig. 1I and J) and orthotopic (Supplementary Fig. S4A and S4B) tumors treated with MRTX1133 for 7 days. Notably, this population has been reported to restrain tumor growth in PDAC (35–37), raising the possibility that this increase in myCAFs may contribute to the antitumor effects of MRTX1133.

Although a small percentage of patients with PDAC exhibit hypervascular tumors, the majority of PDAC tumors are hypovascular (24, 38). To assess the effects of MRTX1133 on tumor vasculature, we stained tumors for the endothelial cell marker endomucin (EMCN). Subcutaneous MRTX1133-treated tumors exhibited an increase in tumor vasculature compared with vehicle controls (Fig. 1K and L). A similar increase in vessel density was not observed in orthotopic MRTX1133-treated tumors, however (Supplementary Fig. S4C and S4D)—a finding that may relate to the greater vascularity of orthotopic tumors at baseline.

Figure 1. Pharmacologic inhibition of KRAS^{G12D} inhibits tumor growth and elicits changes in the tumor stroma in immunocompetent implantation PDAC models. **A**, Tumor volume (mm³) of vehicle- and MRTX1133-treated subcutaneous tumors (6419c5). Growth curves show change in tumor volume over 7 days of treatment. *n* = 10/group. Each symbol represents the average tumor volume. Error bars, SEM. Statistics were determined using a two-way ANOVA with the Sidak multiple comparisons test with significance indicated (****, *P* < 0.0001). Results are representative of 3 independent experiments. **B**, Tumor volume (mm³) of vehicle and MRTX1133-treated subcutaneous tumors (2838c3). Growth curves show change in tumor volume over 7 days of treatment. *n* = 7–8/group. Each symbol represents the average tumor volume. Error bars, SEM. Statistics were determined using a two-way ANOVA with the Sidak multiple comparisons test with significance indicated (****, *P* < 0.0001). Results are representative of 2 independent experiments. **C**, Waterfall plot of vehicle- and MRTX1133-treated orthotopic tumors (6419c5) showing a change in tumor volume after 7 days of treatment compared with baseline at day 0. Each bar represents a single tumor. *n* = 5–6/group. **D**, Representative coimmunofluorescence images of staining for Ki-67 (proliferation marker), GFP (tumor cell marker), and DAPI (nuclear counterstain) in vehicle- and MRTX1133-treated tumors (top). Quantitation of proliferating tumor cells (Ki-67 of GFP⁺) as a percent area per high-power field (HPF) in vehicle-treated (*n* = 3) and MRTX1133-treated (*n* = 4; bottom) tumors. At least 3 fields of view were averaged per tumor. *P* values were determined by an unpaired Student *t* test. Scale bars, 100 μ m. Objective, 20 \times . **E**, Representative coimmunofluorescence images of CC3, GFP, and DAPI in vehicle- and MRTX1133-treated tumors (top). Quantitation of apoptotic tumor cells (CC3 of GFP⁺) as percent area per HPF in vehicle-treated (*n* = 3) and MRTX1133-treated (*n* = 4; bottom) tumors. At least 3 fields of view were averaged per tumor. *P* values were determined by an unpaired Student *t* test. Scale bars, 100 μ m. Objective, 20 \times . **F**, Representative images of H&E staining of subcutaneous tumors (6419c5) following 7 days of treatment with vehicle or MRTX1133. Scale bars, 100 μ m. Objective, 10 \times . **G**, Representative images of Masson's trichrome staining of vehicle- and MRTX1133-treated tumors. Scale bars, 100 μ m. Objective, 10 \times . **H**, Quantitation of collagen deposition (blue stain) as percent area per HPF in vehicle-treated (*n* = 5) and MRTX1133-treated (*n* = 5) tumors. At least 3 fields of view were averaged per tumor. *P* values were determined by an unpaired Student *t* test. Error bars, SD. **I**, Representative coimmunofluorescence images of α SMA, GFP, and DAPI in vehicle- and MRTX1133-treated tumors. Scale bars, 100 μ m. Objective, 20 \times . **J**, Quantitation of fibroblasts (α SMA⁺) as percent area per HPF in vehicle-treated (*n* = 4) and MRTX1133-treated (*n* = 4) tumors. At least 3 fields of view were averaged per tumor. *P* values were determined by Student unpaired *t* test. Error bars, SD. **K**, Representative coimmunofluorescent images of EMCN, GFP, and DAPI in vehicle- and MRTX1133-treated tumors. Scale bars, 100 μ m. Objective, 20 \times . **L**, Quantitation of endothelial cells (EMCN⁺) as percent area per HPF in vehicle-treated (*n* = 4) and MRTX1133-treated (*n* = 4) tumors. At least 3 fields of view were averaged per tumor. *P* values were determined by an unpaired Student *t* test. Error bars, SD.

MRTX1133 Exerts *In Vivo* Effects Early in Treatment

Given the rapidity with which MRTX1133 inhibited tumor growth (Fig. 1A), we next assessed the effect of short-term MRTX1133 treatment. To this end, we administered 3 doses of MRTX1133 over 36 hours and stained YFP⁺ tumor cells for the cell proliferation and cell death markers Ki-67 and CC3. Reduced staining for Ki-67 was observed after 36 hours of treatment (Supplementary Fig. S5A and S5B), consistent with our findings regarding cell proliferation following 7 days of treatment (Fig. 1D). In addition, we observed increased staining for CC3 after 36 hours of treatment (Supplementary Fig. S5C and S5D), contrasting with the minimal increase in cell death observed following 7 days of treatment (Fig. 1E). In addition, we observed a significant accumulation of α SMA⁺ myCAFs (Supplementary Fig. S5E and S5F) and EMCN⁺ endothelial cells (Supplementary Fig. S5G and S5H) after 36 hours of treatment.

To better assess the impact of these effects on tumor growth, we examined two additional cohorts of tumor-bearing mice treated with MRTX1133 or vehicle for 36 hours. Whereas most vehicle-treated tumors grew over this short time interval, MRTX1133-treated tumors exhibited either static growth or reductions in tumor volume (Supplementary Fig. S5I and S5J), which translated to a reduction in tumor mass over a 2-day time period (Supplementary Fig. S5K). These results suggest that MRTX1133 causes a reduction in cell proliferation and an increase in cell death early in treatment, resulting in tumor regression, whereas the apoptosis-inducing activities of the drug may diminish over time.

KRAS^{G12D} Inhibition Alters the Tumor Immune Microenvironment

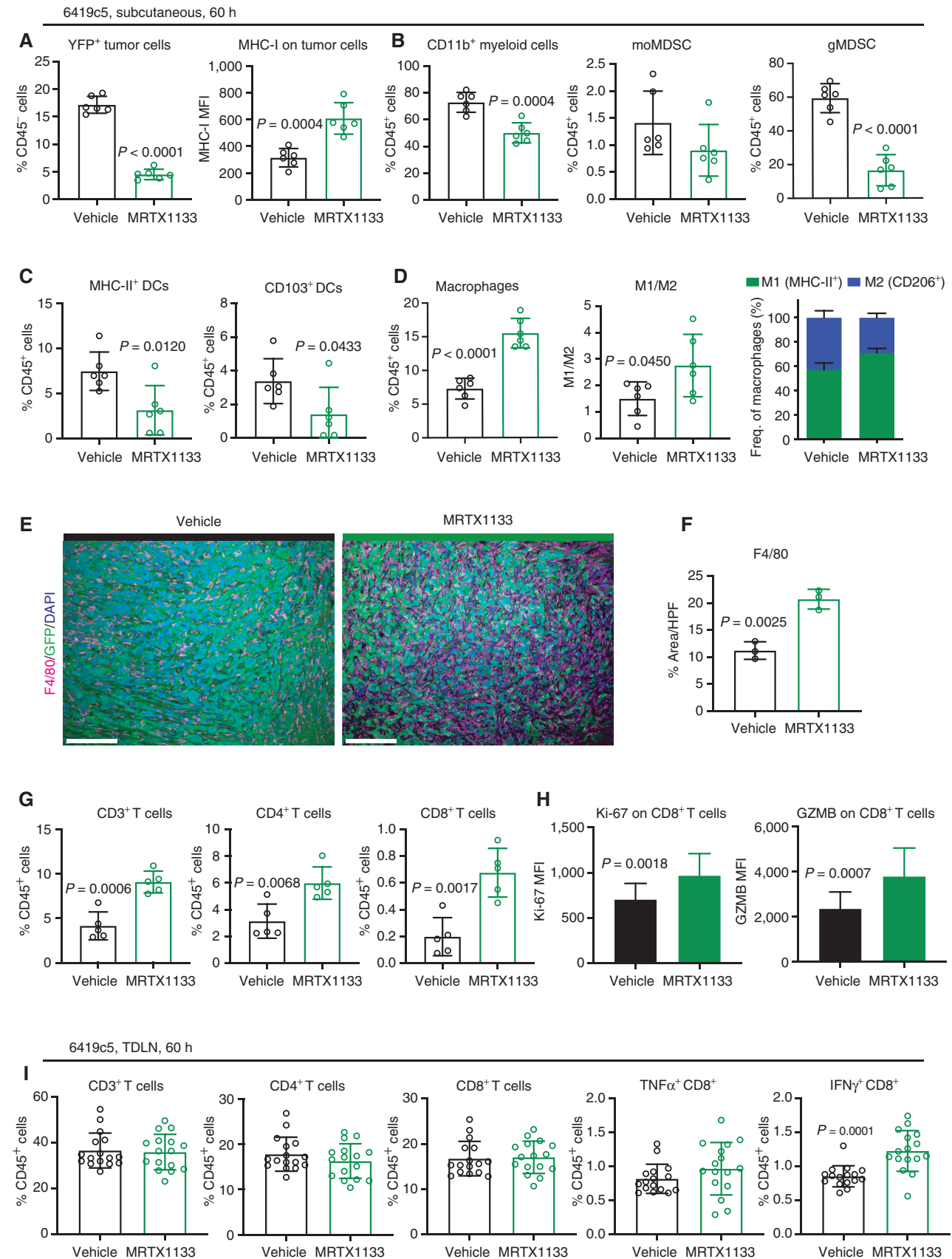
Genetic models using an inducible Kras^{G12D} (iKras) system (9) have revealed changes in the tumor immune microenvironment upon Kras “deinduction,” including an alteration in macrophage polarization with an increase in tissue-repair macrophages (11, 13). However, these Kras deinduction studies failed to reveal changes to T-cell infiltration in the early stages of PDAC (11, 13). To investigate the effects of Kras^{G12D} inhibition with MRTX1133 on tumoral immune infiltration, we performed immune phenotyping of subcutaneous 6419c5 PDAC tumors after 5 doses of MRTX1133 (60 hours) using a flow cytometry immune panel (Supplementary Table S1). First, we confirmed the loss of YFP⁺ tumor cells with Kras^{G12D} inhibition; notably, the tumor cells that survived exhibited

higher expression of MHC class I (Fig. 2A). Within the myeloid compartment, MRTX1133 treatment resulted in a reduction in total myeloid cells (CD45⁺ CD11b⁺), granulocytic myeloid-derived suppressor cells (gMDSC; Ly-6G⁺/Ly-6C^{lo}; Fig. 2B), and dendritic cells (DC; CD11c⁺, MHC-II⁺, and CD11c⁺ CD103⁺; Fig. 2C). We also observed a significant increase in macrophages (CD11b⁺ and F4/80⁺) in Kras^{G12D}-inhibited tumors (Fig. 2D), which we confirmed by staining sections from subcutaneous tumors at 60 hours (Fig. 2E and F) and 7 days (Supplementary Fig. S6A and S6B). To further assess macrophage phenotypes after MRTX1133 treatment, we used flow cytometry to assess the ratio of intratumoral M1-like (CD206^{lo} MHC-II^{hi}) and M2-like (CD206^{hi} MHC-II^{lo}) macrophages (39) as a percentage of total macrophages (CD11b⁺, F4/80⁺, and Ly-6G⁺). This revealed an increase in the M1/M2 ratio in MRTX1133-treated tumors compared with vehicle (Fig. 2D), suggesting Kras^{G12D} inhibition skews macrophage phenotypes to an M1-like state.

Next, to identify potential tumor-derived factors leading to alterations in the TME, we performed cytokine profiling of conditioned media from vehicle- or MRTX1133-treated tumor cells (Supplementary Fig. S6C). Among factors present at detectable levels, we observed a decrease in GM-CSF secretion and an increase in CCL2 secretion from tumor cells treated with MRTX1133 (Supplementary Fig. S6C and S6D). CCL2 is known to recruit CCR2⁺ macrophages in PDAC (40). GM-CSF is known to promote the expansion of MDSCs, whereas its loss abrogates MDSC accumulation in the PDAC TME (41). These data raise the possibility that MRTX1133 treatment alters the macrophage and gMDSC composition of the TME by dysregulating the release of these two factors.

Finally, we assessed the effect of MRTX1133 treatment on the abundance of intratumoral T cells. We identified a significant increase in tumor-infiltrating T cells (CD3⁺), CD4⁺, and CD8⁺ T-cell subsets after 5 doses of MRTX1133 over 60 hours (Fig. 2G). The increase in CD8⁺ T cells was confirmed by immunofluorescence staining for CD8 (Supplementary Fig. S6E and S6F). Additionally, the CD8⁺ T cells expressed higher levels of the proliferation marker Ki-67 and the cytotoxicity marker GZMB after MRTX1133 treatment (Fig. 2H). However, this increase in T-cell infiltration was no longer evident after 7 days of MRTX1133 treatment (Supplementary Fig. S6G), suggesting that T-cell infiltration in response to Kras^{G12D} inhibition is highly dynamic. Further, we assessed T-cell infiltration in the tumor-draining lymph node (TDLN), a major site of T-cell priming. Although there was no difference in total T-cell numbers (CD4⁺ and CD8⁺), there was a

Figure 2. KRAS^{G12D} inhibition alters the tumor immune microenvironment. **A–D**, Flow cytometry of indicated cell subsets from 6419c5 (subcutaneous) tumors after 5 doses over 60 hours of vehicle ($n = 6$) or MRTX1133 ($n = 6$). Ratio of M1-like (MHC-II⁺) to M2-like (CD206⁺) macrophages in 6419c5 (subcutaneous) tumors after 5 doses of vehicle or MRTX1133 (**D**, middle). M1/M2 ratio plotted as the frequency (freq.) of total macrophages (**D**, right). *P* values were determined by an unpaired Student *t* test. Error bars, SD. MFI, mean fluorescence intensity; moMDSC, monocytic myeloid-derived suppressor cell. **E**, Representative coimmunofluorescent images of F4/80, GFP, and DAPI in vehicle- and MRTX1133-treated tumors (6419c5, subcutaneous, 60 hours). Scale bars, 100 μ m. Objective, 20 \times . **F**, Quantitation of macrophages (F4/80⁺) as percent area per high-power field in vehicle-treated ($n = 3$) and MRTX1133-treated ($n = 3$) tumors. At least 3 fields of view were averaged per tumor. *P* values were determined by an unpaired Student *t* test. Error bars, SD. **G**, Flow cytometry of T-cell subsets from 6419c5 (subcutaneous) tumors after 5 doses over 60 hours of vehicle ($n = 5$) or MRTX1133 ($n = 5$). *P* values were determined by an unpaired Student *t* test. Error bars, SD. **H**, Flow cytometry of T-cell subsets from 6419c5 (subcutaneous) tumors after 5 doses over 60 hours of vehicle ($n = 15$) or MRTX1133 ($n = 16$). MFI of Ki-67 and GZMB on CD8⁺ T cells. *P* values were determined by an unpaired Student *t* test. Error bars, SD. **I**, Flow cytometry of T-cell subsets from 6419c5 (subcutaneous) TDLNs after 5 doses over 60 hours of vehicle ($n = 16$) or MRTX1133 ($n = 16$). *P* values were determined by an unpaired Student *t* test. Error bars, SD.



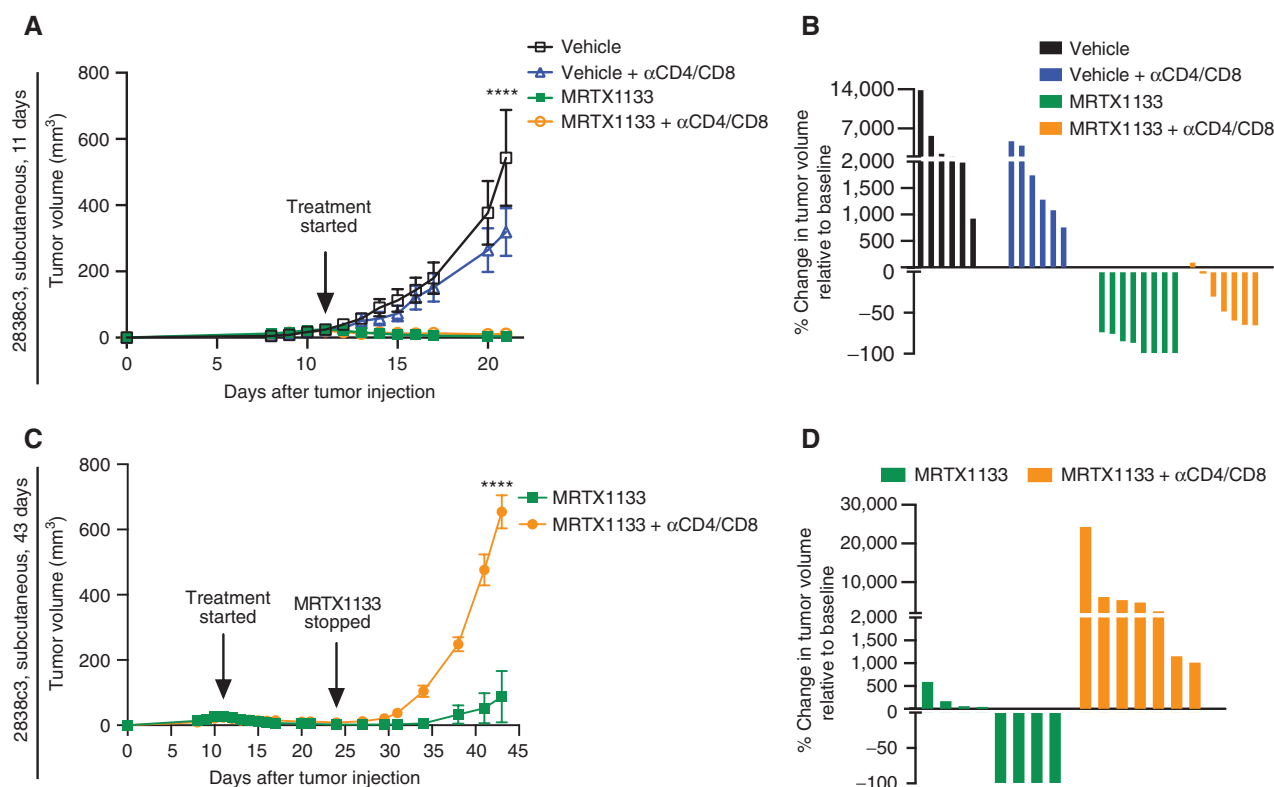


Figure 3. T cells contribute to the antitumor effects of MRTX1133. **A**, Tumor volumes (mm³) of vehicle-, vehicle + αCD4/CD8-, MRTX1133-, and MRTX1133 + αCD4/CD8-treated tumors (2838c3, subcutaneous). Growth curves show changes in tumor volume over 11 days of treatment. *n* = 7–8/group. Each symbol represents the average tumor volume. Error bars, SEM. *P* values were determined using a two-way ANOVA with the Sidak multiple comparisons test with significance indicated (****, *P* < 0.0001). Results representative of 2 independent experiments. **B**, Waterfall plot of vehicle-, vehicle + αCD4/CD8-, MRTX1133-, and MRTX1133 + αCD4/CD8-treated tumors showing changes in tumor volume after 11 days of treatment. Each bar represents a single tumor. *n* = 6–8/group. **C**, Tumor volumes (mm³) of MRTX1133- and MRTX1133 + αCD4/CD8-treated tumors (2838c3, subcutaneous). Growth curves show changes in tumor volume over 14 days of MRTX1133 treatment and subsequent 43 days of T-cell depletion. *n* = 7–8/group. Each symbol represents the average tumor volume. Error bars, SEM. Statistics were determined using a two-way ANOVA with the Sidak multiple comparisons test with significance indicated (****, *P* < 0.0001). Results are representative of 2 independent experiments. **D**, Waterfall plot of MRTX1133- and MRTX1133 + αCD4/CD8-treated tumors showing changes in tumor volume after the removal of MRTX1133. Each bar represents a single tumor. *n* = 7–8/group.

significant increase in IFN γ ⁺ CD8⁺ T cells with MRTX1133 treatment (Fig. 2I). These data suggest Kras^{G12D} inhibition has a systemic effect and enhances CD8⁺ T-cell effector cytokine production within the TDLNs. Taken together, these results suggest that MRTX1133 treatment leads to a reduction in the number of tumor-infiltrating MDSCs, an increase in M1-like macrophages, and an increase in tumor-infiltrating, cytotoxic T cells.

T Cells Contribute to the Antitumor Effects of MRTX1133

To evaluate the contribution of T cells to the antitumor effect of MRTX1133, we performed a T-cell depletion experiment using tumors derived from PDAC clone 2838c3, which gives rise to T cell-inflamed tumors (30). Mice were randomized into 4 arms (vehicle, vehicle + αCD4/CD8, MRTX1133, and MRTX1133 + αCD4/CD8). T-cell depletion was confirmed via flow cytometry (Supplementary Fig. S6H). As expected, treatment with MRTX1133 alone significantly inhibited tumor growth compared with the vehicle group (Fig. 3A), with regressions observed in 8 of 8 (100%) tumors (Fig. 3B). MRTX1133-treated tumors in the absence

of T cells also exhibited significant tumor inhibition, with 6 of 7 (86%) tumors regressing (Fig. 3A and B). Notably, although 4 of 8 (50%) 2838c3 tumors exhibited CRs following MRTX1133 treatment, consistent with our prior results with this cell clone (Fig. 1B; Supplementary Fig. S2F), no CRs were observed in the T-cell depletion cohort (Fig. 3B). These results suggest that T cells are not required for the response to MRTX1133 but instead may augment the extent of the drug's antitumor activity.

Given these findings, we asked whether T cells had the ability to control tumor growth after a course of MRTX1133 treatment. To this end, we stopped MRTX1133 treatment after 14 days in both treatment arms (green and orange tumors in Fig. 3A and B) but continued to deplete T cells in the αCD4/CD8 cohort (orange lines in Fig. 3A and B). By day 43 of the study (3 weeks off drug), 4 of 8 (50%) tumors in the MRTX1133-alone group remained in remission, with no detectable tumors, whereas 4 of 8 (50%) exhibited limited regrowth (Fig. 3C and D). In comparison, 7 of 7 (100%) tumors in the MRTX1133 + αCD4/CD8 arm exhibited substantial regrowth (Fig. 3C and D). These data suggest that T cells contribute to the antitumor effects of MRTX1133 by

constraining tumor regrowth following an initial response to the drug.

KRAS^{G12D} Inhibition Promotes Tumor Regressions in the Autochthonous KPC/Y Model

To determine the efficacy of MRTX1133 in an autochthonous setting, we utilized the stochastic KPC/Y PDAC mouse model (22, 23). KPC/Y mice were screened for tumors by serial palpation and ultrasound of the pancreas and randomized to receive MRTX1133 or vehicle when their tumors reached 20 to 80 mm³. Mice were treated with MRTX1133 for 14 days with weekly ultrasound scans to monitor tumor growth (Fig. 4A). At the end of the 14-day treatment, KPC/Y animals treated with MRTX1133 exhibited a significant inhibition of tumor growth as compared with control animals (Fig. 4B). Tumor regressions were identified in 12 of 13 (92%) of the MRTX1133-treated animals, including 4 animals whose tumors were below the limit of detection by ultrasound.

To assess the role of T cells on the antitumor effects of MRTX1133 in the KPC/Y model, we enrolled an additional cohort of tumor-bearing animals (20–80 mm³, as above) and treated them with MRTX1133 + α CD4/CD8 T cell-depleting antibodies. Similar to our findings in the subcutaneous setting, 13 of 13 (100%) KPC/Y tumors regressed in the absence of T cells (Fig. 4A and B), suggesting that MRTX1133 is not dependent on T cells for its dominant antitumor effects in this model.

We further sought to determine whether T cells contributed to the durability of the antitumor response in autochthonous tumors, as it did in the implantable setting (Fig. 3C and D). To this end, we stopped MRTX1133 treatment after 14 days but continued T-cell depletion for an additional 3 weeks (Fig. 4C). By day 35 of the study (3 weeks off MRTX1133), tumors from the MRTX1133 + α CD4/CD8 arm exhibited increased tumor growth compared with the MRTX1133-alone arm (Fig. 4C; Supplementary Fig. S7A). These data mirror our findings in the implantable setting and provide further evidence that T cells augment the antitumor effect of MRTX1133 in the KPC/Y model.

Recent work has shown disease control is lost after MRTX1133 treatment is discontinued in xenograft models (25). To further assess the durability of MRTX1133 in the presence of T cells, we continued following KPC/Y animals after their 14-day MRTX1133 treatment regimen. Tumor remission in KPC/Y animals lasted between 2 and 4 weeks in 5 of 7 animals (Fig. 4D). Mouse 10527 relapsed 7 weeks after therapy (Fig. 4D). At this time, we resumed MRTX1133 treatment and again saw tumor regression after 1 week of treatment, suggesting that tumor regrowth was due to the removal of the drug rather than acquired resistance. We continued treatment for an additional 7 weeks before tumor relapse was identified (Fig. 4D). These data highlight the relapse variability when MRTX1133 treatment is stopped in the KPC/Y model.

Next, we examined the effects of MRTX1133 on the TME in the autochthonous KPC/Y model. Using immunofluorescence staining, we confirmed a significant loss of p-ERK1/2 in MRTX1133-treated KPC/Y tumors (Fig. 4E and F), suggesting effective inhibition of MAPK signaling. We then

assessed TME changes by staining for α SMA⁺ fibroblasts and F4/80⁺ macrophages (Fig. 4G). We identified an increase in macrophages after MRTX1133 treatment similar to our findings in both subcutaneous and orthotopic settings; however, there was not a significant difference in α SMA⁺ fibroblasts (Fig. 4G and H).

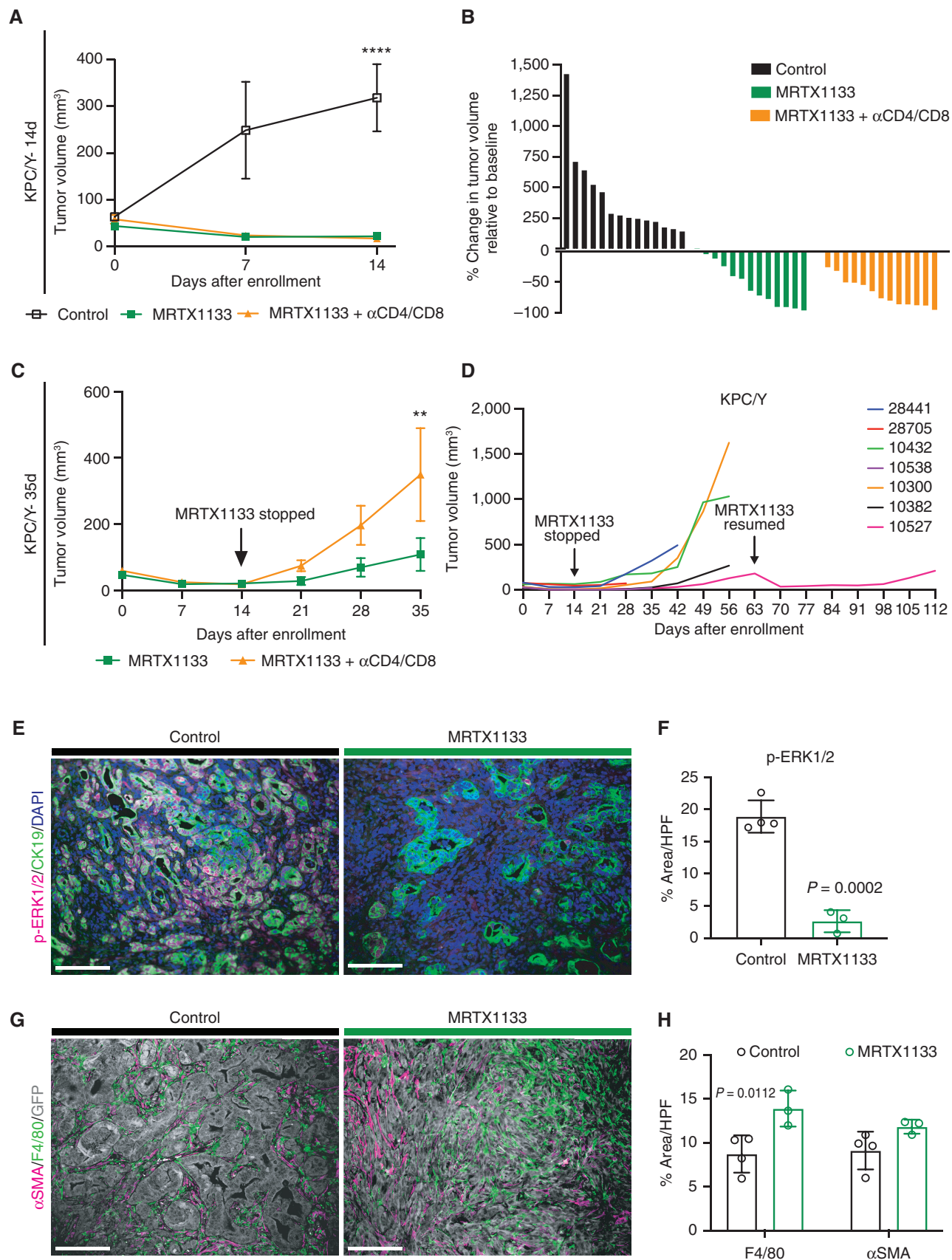
DISCUSSION

Our findings demonstrate that the KRAS^{G12D} inhibitor MRTX1133 exerts potent, specific, and rapid antitumor activity in implantable and autochthonous KRAS^{G12D} mouse models, including the highly treatment-refractory KPC/Y model. In our 10 years of experience testing multiple compounds for antitumor effects in this autochthonous model (37, 42–46), the frequency and depth of tumor regressions observed with MRTX1133 are the most prominent yet observed for any compound or compounds. The dominant effects are likely mediated by cancer cell-intrinsic mechanisms, principally inhibition of ERK1/2 phosphorylation. Nevertheless, the drug also prompts changes in the TME, which may contribute to the antitumor effect, including increases in tumor-associated macrophages (with the adoption of an M1-like phenotype) and α SMA⁺ myofibroblasts—cell types known to mediate tumor inhibitory properties. Our findings also reveal an increase in tumoral T-cell infiltration and a role for T cell-mediated immunity in achieving deeper tumor regressions and sustained disease control. The latter point is critical, as resistance to KRAS^{G12D} inhibitors such as MRTX1133 is likely to limit its clinical effect in patients, as it has for KRAS^{G12C} inhibitors and other targeted therapies.

Effects of MRTX1133 on Tumor Growth

In prior work, MRTX1133 was reported to potently inhibit the growth of multiple human cell lines bearing KRAS^{G12D} mutations at low nanomolar or subnanomolar concentrations (25, 26). We found that MRTX1133 was also active against murine cells bearing *Kras*^{G12D} mutations, albeit with a somewhat lower potency compared with its activity in human cells (IC₅₀ in the 30–160 nmol/L range). Growth inhibition was likely due to perturbations in MAPK signaling, as even low doses of the drug led to a near-complete loss of ERK1/2 phosphorylation. Importantly, murine cells bearing wild-type *Kras*, including an isogenic cell line in which a G12C mutation was substituted for the G12D mutation in the original tumor, were relatively insensitive to MRTX1133.

In vivo, we observed profound growth inhibition of tumors bearing KRAS^{G12D} (but not an isogenic line bearing KRAS^{G12C}) within 36 hours of initial MRTX1133 dose. This effect was associated with a loss of ERK1/2 phosphorylation, reduced proliferation, and an increase in tumor cell apoptosis early but not at later time points. Tumors exhibited a range of responses—from stunted growth to frank regressions and CRs. The response of tumor-bearing KPC/Y animals was particularly notable, as this autochthonous model is refractory to a wide range of small-molecule and immunotherapy regimens. In contrast to the mostly modest antitumor effects that have been previously reported for other compounds in this model, including our own work with immunotherapies (24, 45), the current study produced deep (>50%) or complete



regressions in the majority of tumor-bearing mice. These results contrast sharply with the outcome of vehicle-treated KPC/Y tumors, all of which experienced progression. These findings are consistent with studies utilizing the inducible iKras genetic mouse model (9, 10, 12), in which Kras^{G12D} deinduction resulted in a rapid loss of p-ERK1/2 expression, increased apoptosis, and tumor regressions within 1 week (9, 10, 12). These data suggest that this pharmacologic approach mirrors the antitumor effects observed in genetic models.

Effects of MRTX1133 on the TME

MRTX1133 treatment had multiple effects on the tumor stroma. The most impressive of these was a rapid and sustained increase in intratumoral macrophages, which we confirmed in all models tested by immunostaining. PDAC cells treated with MRTX1133 *in vitro* produced elevated levels of CCL2, nominating this factor as a candidate mediator of the macrophage effect. Macrophage immunophenotyping revealed a shift toward an M1 phenotype, again similar to findings in the inducible iKras mouse model (11, 13), raising the possibility that macrophage-mediated phagocytosis of tumor cells may contribute to the antitumor effects of Kras^{G12D} inhibition. In concordance with our work, recent reports examining the role of Kras^{G12C} inhibitors on the tumor immune microenvironment also identified an increase in M1-like macrophages, a loss of MDSCs, and dependency on a functional immune system (14, 47).

Treatment with MRTX1133 also resulted in a reproducible increase in the area occupied by α SMA⁺ myofibroblasts and collagen across the various tumor models studied, with a trend toward more myofibroblasts in the KPC/Y model. As α SMA⁺ fibroblasts restrain tumor growth in PDAC (35–37), an increase in this CAF subpopulation may also contribute to the antitumor effects of the drug. Our findings contrast with those observed in the genetic iKras model, in which Kras^{G12D} deinduction led to a loss of α SMA⁺ fibroblasts (9–11). However, those iKras studies were performed at the pancreatic intraepithelial neoplasia stage rather than in established tumors, and thus Kras^{G12D} inhibition may affect stromal cells in a stage-specific manner.

Our studies revealed other changes in the TME following MRTX1133 treatment, including a decreased abundance of gMDSCs and an increased abundance of EMCN⁺ endothelial cells, which may have had additional effects on tumor

growth. However, these effects were less reproducible across the models tested. For example, the effect on endothelial cells was dramatic in the subcutaneous setting, modest in the orthotopic setting, and undetectable in the autochthonous setting. One possible explanation for this variability is that baseline blood vessel density differs across models. Further work is required to elucidate the vasculature changes identified with MRTX1133 treatment.

Durability of Response

Because acquired resistance is a near-universal feature of targeted therapies (48, 49), including KRAS^{G12C} inhibition (50), we estimated the durability of MRTX1133-induced tumor regressions. For animals treated with MRTX1133 for just 14 days and then observed in the subcutaneous model, nearly all animals achieving CR at the completion of therapy remained disease free nearly 3 weeks later. Although a few mice were refractory to MRTX1133 treatment, we did not observe tumor regrowth (relapses) while on treatment in mice that had exhibited tumor regressions. In the autochthonous KPC/Y model, several animals with deep tumor regressions did not exhibit tumor regrowth for 3 weeks or more following cessation of MRTX1133 treatment. Thus, although we observed striking antitumor effects overall, we also observed examples of primary refractoriness and post-treatment relapses.

T Cells Augment the Antitumor Effects of MRTX1133

PDAC tumors remained sensitive to MRTX1133 despite T-cell depletion in all models tested. These results suggest that T cells are not required for the drug's principal antitumor activity. However, several lines of evidence suggest that T cells are critical for achieving deeper and more durable remissions: (i) In our implantation experiments using three PDAC cell lines, only the T cell-inflamed tumor line (2838c3) achieved CRs; (ii) MRTX1133 treatment prompted a rapid (<3 days) increase in intratumoral T cells; (iii) T-cell depletion abrogated the ability of 2838c3 tumors to achieve CRs; and (iv) T-cell depletion, in both implantable and autochthonous settings, was associated with more rapid tumor regrowth following a 14-day course of MRTX1133, whereas tumors with an intact T-cell compartment remained small or undetectable. Thus, T-cell responses induced by MRTX1133 may contribute to the durability of regressions.

Figure 4. KRAS^{G12D} inhibition promotes tumor regressions in the autochthonous KPC/Y model. **A**, Tumor volumes (mm³) of KPC/Y tumors treated with vehicle control, MRTX1133, or MRTX1133 + α CD4/CD8. Growth curves show changes in tumor volume over 14 days of MRTX1133 treatment. $n = 13$ –14/group. Each symbol represents the average tumor volume. Error bars, SEM. Statistics were determined using a two-way ANOVA with the Sidak multiple comparisons test with significance indicated (***, $P < 0.0001$). **B**, Waterfall plot of KPC/Y tumors in **A** treated with vehicle, MRTX1133, or MRTX1133 + α CD4/CD8 showing changes in tumor volume after 14 days of treatment. Each bar represents a single tumor. $n = 13$ –14/group. **C**, Tumor volumes (mm³) of MRTX1133 and MRTX1133 + α CD4/CD8-treated KPC/Y tumors. Growth curves show changes in tumor volume over 14 days of MRTX1133 treatment and an additional 3 weeks of α CD4/CD8 in the T-cell depletion cohort. $n = 6$ –8/group. Each symbol represents average tumor volume. Error bars, SEM. Statistics were determined using a two-way ANOVA with the Sidak multiple comparisons test with significance indicated (**, $P < 0.01$). **D**, Tumor volumes (mm³) of KPC/Y tumors ($n = 7$) treated with MRTX1133. Growth curves show changes in tumor volume over 14 days of MRTX1133 treatment and an additional 6 weeks off therapy. One mouse (10527) resumed MRTX1133 treatment at 63 days after enrollment and continued treatment for an additional 7 weeks. Each line represents a single tumor. **E**, Representative coimmunofluorescence images of p-ERK1/2, CK19, and DAPI in vehicle- and MRTX1133-treated KPC/Y tumors. Scale bars, 100 μ m. Objective, 20 \times . **F**, Quantitation of p-ERK1/2 staining as percent area per high-power field (HPF) in control-treated ($n = 4$) and MRTX1133-treated ($n = 3$) KPC/Y tumors. At least 3 fields of view were averaged per tumor. P values were determined by an unpaired Student t test. Error bars, SD. **G**, Representative coimmunofluorescence images of α SMA, F4/80, and GFP in control- and MRTX1133-treated KPC/Y tumors. Scale bars, 100 μ m. Objective, 20 \times . **H**, Quantitation of macrophages (F4/80⁺) and fibroblasts (α SMA⁺) as percent area per HPF in control-treated ($n = 4$) and MRTX1133-treated ($n = 3$) KPC/Y tumors. At least 3 fields of view were averaged per tumor. P values were determined using a two-way ANOVA with the Sidak multiple comparisons test. Error bars, SD.

One possible explanation for these results is a “vaccine effect,” whereby profound tumor cell death induced by Kras^{G12D} inhibition leads to antigen release and T-cell priming. Although chemotherapy and radiation have also been used to activate an antitumor immune response by inducing tumor cell death, these treatments are also associated with T-cell dysfunction and toxicity. In that respect, MRTX1133 may represent a major improvement over traditional “vaccine effects,” because its activity is specific for cells carrying Kras^{G12D}, thus sparing the antitumor immune response.

Summary

Pharmacologic inhibition of KRAS^{G12D} in pancreatic cancer models has specific, potent, and durable effects in promoting tumor regression, which, in the absence of overt toxicity, suggests that this and similar inhibitors should be tested as potential, high-impact novel therapies for patients with PDAC. These approaches will complement other strategies that leverage the ability of Kras^{G12D} to serve as a neoantigen using engineered autologous T cells (51, 52). Our study highlights the importance of exploiting the breadth of tumor biology orchestrated by mutant KRAS, particularly the immune system, to devise rational combinations leading to long-term patient responses.

METHODS

Animals

Female wild-type C57BL/6 mice were purchased from The Jackson Laboratory (000664) and used between 6 and 8 weeks of age. *Kras*^{LSL-G12D/+}; *Trp53*^{LSL-R172H/+}; *Pdx1-Cre*; *Rosa26*^{YFP/YFP} (KPC/Y; ref. 23) mice were bred and maintained in specific pathogen-free facilities at the University of Pennsylvania. For KPC/Y experiments, both male and female mice were used to control for sex as a biological variable. Experiments were randomized but not blinded. All animal experiments and procedures were performed under approved protocols in accordance with guidelines from the university's Institutional Animal Care and Use Committee.

Tumor Cell Lines

Murine PDAC cell lines were derived from tumor-bearing KPC/Y (6419c5, 2838c3; ref. 30) or KPC (4662; ref. 29) animals on a congenic C57BL/6 background. C57BL/6 murine LLC and colon adenocarcinoma MC38 (28) cell lines were obtained from ATCC and Dr. Dimitry Gabrilovich (The Wistar Institute), respectively. Cells were cultured in Dulbecco's modified Eagle medium DMEM (high glucose without sodium pyruvate) supplemented with 10% heat-inactivated fetal bovine serum (FBS), and 1% penicillin/streptomycin. Human PDAC cell lines (BxPC-3, AsPC-1, and MIA PaCa-2) were purchased from ATCC. Cell lines were maintained according to ATCC guidelines. The 4662-G12C line was generated using CRISPR/Cas9 technology to remove the endogenous G12D mutation and instead express the G12C mutation using lentiviral transduction. Cell lines were routinely tested for *Mycoplasma* using the MycoAlert Mycoplasma Detection Kit (Lonza, LT07-318). Three murine KRAS^{G12D} lines were used (4662, 6419c5, and 2838c3). One murine KRAS^{G12C} (LLC) line and one murine wild-type KRAS (MC38) line were used. One human KRAS^{G12D} (AsPC-1) line, one human KRAS^{G12C} (MIA PaCa-2) line, and one human wild-type KRAS (BxPC-3) line were used. Kras allele status (wild-type, G12D, G12C) was confirmed by genomic sequencing.

Cell Viability Assay

To determine IC₅₀ values, 2 to 5 × 10³ tumor cells were plated in a 96-well plate. Cells were treated 24 hours later with DMSO or

serial dilutions of MRTX1133. Cell viability was read 72 hours later using CellTiter-Glo (Promega, G7571). All reagents and plates were brought to room temperature before measuring viability. An equal volume of CellTiter-Glo was then added to each well. The cells were lysed, and the plate was incubated for 10 minutes at room temperature. Luminescence values were recorded, and IC₅₀ values were generated using GraphPad Prism (RRID:SCR_002798) version 9.1.2.

Western Blot Analysis

Cells were washed with ice-cold PBS, and lysate was generated using RIPA buffer. Equal amounts of protein were run in reducing conditions on SDS-PAGE gels and then transferred to a PVDF membrane. Membranes were blocked at room temperature for 1 hour in a blocking buffer (LI-COR). After blocking, membranes were incubated in primary antibody diluted in an antibody diluent buffer (LI-COR) overnight at 4°C. After 3 washes in PBS-T, membranes were incubated at room temperature for 1 hour with fluorescence-conjugated secondary antibodies (LI-COR) diluted in Antibody Diluent Buffer. α -Tubulin (Cell Signaling Technology, 3873) was used as a loading control. Primary antibodies for Western blot included anti-p-ERK (Cell Signaling Technology, 4370), and anti-ERK (Cell Signaling Technology, 4695).

Tumor Cell Implantation

A single-cell suspension of murine PDAC cells was prepared in DMEM and kept on ice until injection. Tumor cells (1 × 10⁵ to 1 × 10⁶) were injected subcutaneously into 6- to 8-week-old C57BL/6 mice. For orthotopic injections, 6.25 × 10⁴ tumor cells were implanted directly into the pancreas as previously described (32).

In Vivo Treatments

MRTX1133 Treatment. For *in vivo* use, MRTX1133 was formulated in 10% research grade Captisol (CyDex Pharmaceuticals) in 50 mmol/L citrate buffer pH 5.0 (Teknova, Q2443). Once formulated, MRTX1133 was protected from light and stored at 4°C for 1 week. MRTX1133 was administered at 30 mg/kg via i.p. injection with b.i.d. dosing, which was defined as the maximum tolerated dose and was well tolerated with no overt signs of toxicity and only minor weight loss early in treatment (Supplementary Fig. S7B–S7D), consistent with earlier observations (25, 26).

T-cell Depletion. Once tumors reached an average volume of 20 to 50 mm³, MRTX1133 (30 mg/kg) or vehicle was administered i.p. b.i.d. for 2 weeks. CD4⁺ and CD8⁺ T-cell depletion started 1 day before initiating MRTX1133 treatment and continued twice a week for the remainder of the experiment. Depleted mice received 200 μ g of CD4⁺ (Bio X Cell, GK1.5) and CD8⁺ (Bio X Cell, 2.43) antibodies i.p., whereas control mice were given isotype control (Bio X Cell, LTF-2). Peripheral blood was collected to confirm CD4⁺ and CD8⁺ T-cell depletion via flow cytometry.

Tumor Growth Analysis

Subcutaneous tumor measurements began when tumors became palpable. Subcutaneous tumors were measured daily with digital calipers for short-term experiments (every 2–3 days for longer experiments). Subcutaneous tumor volume was calculated as (W² × L)/2. Orthotopic and KPC/Y tumors were measured by ultrasound once per week. Animals were randomized into treatment groups when tumors reached 20 to 80 mm³. Mice with tumors >100 mm³ were not included in the study. Waterfall plots were calculated using the baseline tumor volume on day 0 compared with tumor volume at the end of the experiment. The percent change in tumor volume was calculated by ((final volume – initial volume)/initial volume) × 100. A tumor with –100% change from baseline was considered to have a CR.

Tail-Vein Metastasis Assay

Murine PDAC cells were resuspended in DMEM. Cells (1×10^5) were injected in 200 μ L of DMEM via tail vein into 6- to 8-week-old C57BL/6 mice. Tumor cells were allowed to settle for 3 days. Mice were treated with either vehicle or MRTX1133 for 7 days. Lungs were harvested and analyzed for YFP signal using a Lecia M216FA fluorescent microscope. FIJI software was used for the quantitation of the YFP signal over the entire area of the lung tissue.

Flow Cytometry Analysis

Mouse tumors were mechanically and enzymatically (2 mg/mL collagenase IV in DMEM) digested for 1 hour at 37°C with shaking. Samples were then washed with DMEM and 10% FBS and filtered through a 70- μ m strainer to obtain a single-cell suspension. Cells were labeled with primary fluorophore-conjugated antibodies and a live/dead stain (Supplementary Table S1) for 20 minutes at 4°C. Cells were washed and resuspended in flow buffer. For quantification of cytokine expression, TDLNs were mechanically processed into single-cell suspensions. The single-cell suspensions were plated at a concentration of ~ 1 to 2 million cells in 1 mL of RP-10 media with 2 \times GolgiPlug (1:50; BD 555029). Cells were stimulated for 2 hours at 37°C with 2 μ L of a cell activation cocktail containing phorbol myristate acetate and ionomycin (BioLegend 423301). Each sample had a matched, unstimulated control. Subsequent washes and staining prior to fixation were performed in solutions containing 1 \times GolgiPlug (1:100) to prevent the release of cytokines. RP-10 media were made by diluting RP-100 media in RPMI complete media. RPMI complete media contained RPMI 1640 with 10% FBS, L-glutamine, and gentamicin, and RP-100 media consisted of RPMI complete media with 0.05 mmol/L 2-Mercaptoethanol. For intracellular staining in tumor and TDLN samples, cells were permeabilized and fixed for 30 minutes at 4°C, washed, and then stained for intracellular markers overnight at 4°C. Data were acquired on an LSR II or Symphony A3 Lite B flow cytometer, with analysis performed using FlowJo (RRID:SCR_008520) version 10.8.1.

IHC Staining and Analysis

After removal, murine tumors were washed 3 \times with PBS. Tissues were then fixed overnight in zinc formalin. After 24 hours, tissues were transferred to 70% ethanol and processed for paraffin embedding. Tissues were sectioned at 5 μ m. H&E and Masson's trichrome stains were performed according to the manufacturer's guidelines. For immunofluorescence staining, slides were deparaffinized and rehydrated through a series of xylene and ethanol washes. Slides underwent antigen retrieval followed by blocking with 5% donkey serum for 1 hour at room temperature. Primary antibodies were added to the slides (Supplementary Table S1) and incubated overnight at 4°C. Slides were then washed 2 \times with PBS-T and incubated with secondary antibodies (Alexa Fluor secondaries, 1:250) for 1 hour at room temperature. Nuclei were counterstained with DAPI (1:1,000). Slides were mounted with aqua-poly/mount and coverslipped. Images were captured using an Olympus IX71 inverted microscope and a DP71 camera; 10 \times , 20 \times , and 40 \times objectives were used and are noted in the figure legends. FIJI software was used for quantitation, with each datapoint an average of 3 to 5 magnification fields per sample.

Cytokine Array

To assess secreted factors, tumor cell conditioned media were collected from 6419c5 cells treated with vehicle or MRTX1133 (20 nmol/L) for 48 hours. Conditioned media were spun at 1,500 rpm to remove debris, and the supernatant was stored at -80°C . Conditioned media were analyzed using the Proteome Profiler kit (R&D Systems, ARY006) according to manufacturer's guidelines. Quantitation was performed using the protein array analyzer macro in FIJI. Measurements were performed in duplicate.

Statistical Analysis

GraphPad Prism (RRID:SCR_002798) version 9.1.2 was used for statistical analyses and graphical representation. Data are presented as means \pm SD or SEM. Two-tailed Student *t* test and two-way ANOVA with multiple corrections were performed for comparison between groups. For IC₅₀ generation, concentrations were log transformed, data were then normalized to control, and log(inhibitor) versus response (three parameters) test was used. A *P* < 0.05 was considered statistically significant.

Data Availability Statement

Data sharing is not applicable, as data for which a community-recognized, structured repository exists (e.g., next-generation sequencing data) were not created or analyzed in this study.

Authors' Disclosures

T.R. Donahue reports other support from Trethera Corporation outside the submitted work. J.G. Christensen reports personal fees, nonfinancial support, and other support from Mirati Therapeutics during the conduct of the study; personal fees and nonfinancial support from Mirati Therapeutics outside the submitted work; and patent 10,633,381 issued to Mirati Therapeutics. R.H. Vonderheide reports other support from Children's Hospital Boston and Novartis outside the submitted work. B.Z. Stanger reports grants from the NIH and nonfinancial support from Mirati Therapeutics during the conduct of the study, as well as personal fees from iTeos Therapeutics, grants and personal fees from Boehringer Ingelheim, and grants from Cour Pharmaceuticals outside the submitted work. No disclosures were reported by the other authors.

Authors' Contributions

S.B. Kemp: Conceptualization, formal analysis, validation, investigation, visualization, writing-original draft, writing-review and editing. **N. Cheng:** Validation, investigation, visualization, writing-review and editing. **N. Markosyan:** Conceptualization, supervision, investigation, visualization, methodology, writing-review and editing. **R. Sor:** Formal analysis, investigation, visualization, writing-review and editing. **I.K. Kim:** Investigation, methodology, writing-review and editing. **J. Hallin:** Conceptualization, resources, writing-review and editing. **J. Shoush:** Formal analysis, validation, investigation, writing-review and editing. **L. Quinones:** Validation, investigation, writing-review and editing. **N.V. Brown:** Formal analysis, validation, investigation, visualization, writing-review and editing. **J.B. Bassett:** Formal analysis, investigation, visualization. **N. Joshi:** Formal analysis, validation, investigation, writing-review and editing. **S. Yuan:** Formal analysis, investigation, visualization, writing-review and editing. **M. Smith:** Investigation, writing-review and editing. **W.P. Vostrejs:** Formal analysis, validation, investigation, visualization, methodology, writing-review and editing. **K.Z. Perez-Vale:** Validation, investigation, visualization, writing-review and editing. **B. Kahn:** Investigation, visualization, writing-review and editing. **F. Mo:** Validation, investigation, writing-review and editing. **T.R. Donahue:** Resources, writing-review and editing. **C.G. Radu:** Resources, writing-review and editing. **C. Clendenin:** Formal analysis, supervision, validation, investigation, project administration, writing-review and editing. **J.G. Christensen:** Conceptualization, resources, writing-review and editing. **R.H. Vonderheide:** Conceptualization, resources, formal analysis, supervision, funding acquisition, validation, investigation, visualization, methodology, writing-original draft, project administration, writing-review and editing. **B.Z. Stanger:** Conceptualization, resources, formal analysis, supervision, funding acquisition, validation, investigation, visualization, methodology, writing-original draft, project administration, writing-review and editing.

Acknowledgments

This study was funded by NIH R01-CA229803 (to R.H. Vonderheide and B.Z. Stanger), R01-CA252225 (to B.Z. Stanger), T32-CA009140 (to S.B. Kemp), and P30-CA016520 (Abramson Cancer Center); the Cancer Research Institute (CRI4097 to S.B. Kemp); the Parker Institute for Cancer Immunotherapy (to R.H. Vonderheide); the Penn Pancreatic Cancer Research Center; and the Abramson Family Cancer Research Institute. We acknowledge Penn's Pancreatic Cancer Mouse Hospital, the Abramson Cancer Center Veterinary Comparative Pathology Shared Resource, and the Molecular Pathology and Imaging Core at the University of Pennsylvania. We thank Woosuk Kim, Luyi Li, and Katelyn T. Byrne for the 4662-G12C line. We are thankful to members of the Stanger and Vonderheide laboratories and members of the scientific staff at Mirati Therapeutics for their comments and suggestions.

The publication costs of this article were defrayed in part by the payment of publication fees. Therefore, and solely to indicate this fact, this article is hereby marked "advertisement" in accordance with 18 USC section 1734.

Note

Supplementary data for this article are available at Cancer Discovery Online (<http://cancerdiscovery.aacrjournals.org/>).

Received September 22, 2022; revised November 9, 2022; accepted November 29, 2022; published first December 6, 2022.

REFERENCES

- Siegel RL, Miller KD, Fuchs HE, Jemal A. Cancer statistics, 2022. *CA Cancer J Clin* 2022;72:7–33.
- Brahmer JR, Tykodi SS, Chow LQ, Hwu WJ, Topalian SL, Hwu P, et al. Safety and activity of anti-PD-L1 antibody in patients with advanced cancer. *N Engl J Med* 2012;366:2455–65.
- Royal RE, Levy C, Turner K, Mathur A, Hughes M, Kammula US, et al. Phase 2 trial of single agent ipilimumab (anti-CTLA-4) for locally advanced or metastatic pancreatic adenocarcinoma. *J Immunother* 2010;33:828–33.
- Conroy T, Desseigne F, Ychou M, Bouche O, Guimbaud R, Becouarn Y, et al. FOLFIRINOX versus gemcitabine for metastatic pancreatic cancer. *N Engl J Med* 2011;364:1817–25.
- Conroy T, Hammel P, Hebbar M, Ben Abdelghani M, Wei AC, Raoul JL, et al. FOLFIRINOX or gemcitabine as adjuvant therapy for pancreatic cancer. *N Engl J Med* 2018;379:2395–406.
- Von Hoff DD, Ervin T, Arena FP, Chiorean EG, Infante J, Moore M, et al. Increased survival in pancreatic cancer with nab-paclitaxel plus gemcitabine. *N Engl J Med* 2013;369:1691–703.
- Hosein AN, Dougan SK, Aguirre AJ, Maitra A. Translational advances in pancreatic ductal adenocarcinoma therapy. *Nat Cancer* 2022;3:272–86.
- Moore AR, Rosenberg SC, McCormick F, Malek S. RAS-targeted therapies: is the undruggable druggable? *Nat Rev Drug Discov* 2020;19:533–52.
- Collins MA, Bednar F, Zhang Y, Brisset JC, Galban S, Galban CJ, et al. Oncogenic Kras is required for both the initiation and maintenance of pancreatic cancer in mice. *J Clin Invest* 2012;122:639–53.
- Collins MA, Brisset JC, Zhang Y, Bednar F, Pierre J, Heist KA, et al. Metastatic pancreatic cancer is dependent on oncogenic Kras in mice. *PLoS One* 2012;7:e49707.
- Velez-Delgado A, Donahue KL, Brown KL, Du W, Irizarry-Negron V, Menjivar RE, et al. Extrinsic KRAS signaling shapes the pancreatic microenvironment through fibroblast reprogramming. *Cell Mol Gastroenterol Hepatol* 2022;13:1673–99.
- Ying H, Kimmelman AC, Lyssiotis CA, Hua S, Chu GC, Fletcher-Sananikone E, et al. Oncogenic Kras maintains pancreatic tumors through regulation of anabolic glucose metabolism. *Cell* 2012;149:656–70.
- Zhang Y, Yan W, Mathew E, Kane KT, Brannon A 3rd, Adoumie M, et al. Epithelial-mesenchymal cell crosstalk regulates acinar cell plasticity and pancreatic remodeling in mice. *Elife* 2017;6:e27388.
- Canon J, Rex K, Saiki AY, Mohr C, Cooke K, Bagal D, et al. The clinical KRAS(G12C) inhibitor AMG 510 drives anti-tumour immunity. *Nature* 2019;575:217–23.
- Hallin J, Engstrom LD, Hargis L, Calinisan A, Aranda R, Briere DM, et al. The KRAS(G12C) inhibitor MRTX849 provides insight toward therapeutic susceptibility of KRAS-mutant cancers in mouse models and patients. *Cancer Discov* 2020;10:54–71.
- Hong DS, Fakih MG, Strickler JH, Desai J, Durm GA, Shapiro GI, et al. KRAS(G12C) inhibition with sotorasib in advanced solid tumors. *N Engl J Med* 2020;383:1207–17.
- Lanman BA, Allen JR, Allen JG, Amegadzie AK, Ashton KS, Booker SK, et al. Discovery of a covalent inhibitor of KRAS(G12C) (AMG 510) for the treatment of solid tumors. *J Med Chem* 2020;63:52–65.
- Skoulidis F, Li BT, Dy GK, Price TJ, Falchook GS, Wolf J, et al. Sotorasib for lung cancers with KRAS p.G12C mutation. *N Engl J Med* 2021;384:2371–81.
- Bailey P, Chang DK, Nones K, Johns AL, Patch AM, Gingras MC, et al. Genomic analyses identify molecular subtypes of pancreatic cancer. *Nature* 2016;531:47–52.
- Waters AM, Der CJ. KRAS: the critical driver and therapeutic target for pancreatic cancer. *Cold Spring Harb Perspect Med* 2018;8:a031435.
- Dougan SK. The pancreatic cancer microenvironment. *Cancer J* 2017;23:321–5.
- Hingorani SR, Wang L, Multani AS, Combs C, Deramaudt TB, Hruban RH, et al. Trp53R172H and KrasG12D cooperate to promote chromosomal instability and widely metastatic pancreatic ductal adenocarcinoma in mice. *Cancer Cell* 2005;7:469–83.
- Rhim AD, Mirek ET, Aiello NM, Maitra A, Bailey JM, McAllister F, et al. EMT and dissemination precede pancreatic tumor formation. *Cell* 2012;148:349–61.
- Olive KP, Jacobetz MA, Davidson CJ, Gopinathan A, McIntyre D, Honess D, et al. Inhibition of Hedgehog signaling enhances delivery of chemotherapy in a mouse model of pancreatic cancer. *Science* 2009;324:1457–61.
- Hallin J, Bowcut V, Calinisan A, Briere DM, Hargis L, Engstrom LD, et al. Anti-tumor efficacy of a potent and selective non-covalent KRAS(G12D) inhibitor. *Nat Med* 2022;28:2171–82.
- Wang X, Allen S, Blake JF, Bowcut V, Briere DM, Calinisan A, et al. Identification of MRTX1133, a noncovalent, potent, and selective KRAS(G12D) inhibitor. *J Med Chem* 2022;65:3123–33.
- Bertram JS, Janik P. Establishment of a cloned line of Lewis lung carcinoma cells adapted to cell culture. *Cancer Lett* 1980;11:63–73.
- Corbett TH, Griswold DP Jr, Roberts BJ, Peckham JC, Schabel FM Jr. Tumor induction relationships in development of transplantable cancers of the colon in mice for chemotherapy assays, with a note on carcinogen structure. *Cancer Res* 1975;35:2434–9.
- Lo A, Wang LS, Scholler J, Monslow J, Avery D, Newick K, et al. Tumor-promoting desmoplasia is disrupted by depleting FAP-expressing stromal cells. *Cancer Res* 2015;75:2800–10.
- Li J, Byrne KT, Yan F, Yamazoe T, Chen Z, Baslan T, et al. Tumor cell-intrinsic factors underlie heterogeneity of immune cell infiltration and response to immunotherapy. *Immunity* 2018;49:178–93.
- Killion JJ, Radinsky R, Fidler IJ. Orthotopic models are necessary to predict therapy of transplantable tumors in mice. *Cancer Metastasis Rev* 1998;17:279–84.
- Hay CA, Sor R, Flowers AJ, Clendenin C, Byrne KT. Ultrasound-guided orthotopic implantation of murine pancreatic ductal adenocarcinoma. *J Vis Exp* 2019;153:e60497.
- Provenzano PP, Cuevas C, Chang AE, Goel VK, Von Hoff DD, Hingorani SR. Enzymatic targeting of the stroma ablates physical barriers to treatment of pancreatic ductal adenocarcinoma. *Cancer Cell* 2012;21:418–29.
- Ohlund D, Handly-Santana A, Biffi G, Elyada E, Almeida AS, Ponz-Sarvis M, et al. Distinct populations of inflammatory fibroblasts and myofibroblasts in pancreatic cancer. *J Exp Med* 2017;214:579–96.

35. Biffi G, Oni TE, Spielman B, Hao Y, Elyada E, Park Y, et al. IL1-induced JAK/STAT signaling is antagonized by TGFβ to shape CAF heterogeneity in pancreatic ductal adenocarcinoma. *Cancer Discov* 2019;9:282–301.
36. Ozdemir BC, Pentcheva-Hoang T, Carstens JL, Zheng X, Wu CC, Simpson TR, et al. Depletion of carcinoma-associated fibroblasts and fibrosis induces immunosuppression and accelerates pancreas cancer with reduced survival. *Cancer Cell* 2014;25:719–34.
37. Rhim AD, Oberstein PE, Thomas DH, Mirek ET, Palermo CF, Sastra SA, et al. Stromal elements act to restrain, rather than support, pancreatic ductal adenocarcinoma. *Cancer Cell* 2014;25:735–47.
38. Kahn BM, Lucas A, Alur RG, Wengyn MD, Schwartz GW, Li J, et al. The vascular landscape of human cancer. *J Clin Invest* 2021;131:e136655.
39. Carretero R, Sektioglu IM, Garbi N, Salgado OC, Beckhove P, Hammerling GJ. Eosinophils orchestrate cancer rejection by normalizing tumor vessels and enhancing infiltration of CD8(+) T cells. *Nat Immunol* 2015;16:609–17.
40. Sanford DE, Belt BA, Panni RZ, Mayer A, Deshpande AD, Carpenter D, et al. Inflammatory monocyte mobilization decreases patient survival in pancreatic cancer: a role for targeting the CCL2/CCR2 axis. *Clin Cancer Res* 2013;19:3404–15.
41. Bayne LJ, Beatty GL, Jhala N, Clark CE, Rhim AD, Stanger BZ, et al. Tumor-derived granulocyte-macrophage colony-stimulating factor regulates myeloid inflammation and T cell immunity in pancreatic cancer. *Cancer Cell* 2012;21:822–35.
42. Aiello NM, Bajor DL, Norgard RJ, Sahmoud A, Bhagwat N, Pham MN, et al. Metastatic progression is associated with dynamic changes in the local microenvironment. *Nat Commun* 2016;7:12819.
43. Markosyan N, Li J, Sun YH, Richman LP, Lin JH, Yan F, et al. Tumor cell-intrinsic EPHA2 suppresses anti-tumor immunity by regulating PTGS2 (COX-2). *J Clin Invest* 2019;129:3594–609.
44. Beatty GL, Chiorean EG, Fishman MP, Saboury B, Teitelbaum UR, Sun W, et al. CD40 agonists alter tumor stroma and show efficacy against pancreatic carcinoma in mice and humans. *Science* 2011;331:1612–6.
45. Rech AJ, Dada H, Kortzin JJ, Henao-Mejia J, Minn AJ, Twyman-Saint Victor C, et al. Radiotherapy and CD40 activation separately augment immunity to checkpoint blockade in cancer. *Cancer Res* 2018;78:4282–91.
46. Winograd R, Byrne KT, Evans RA, Odorizzi PM, Meyer AR, Bajor DL, et al. Induction of T-cell immunity overcomes complete resistance to PD-1 and CTLA-4 blockade and improves survival in pancreatic carcinoma. *Cancer Immunol Res* 2015;3:399–411.
47. Briere DM, Li S, Calinisan A, Sudhakar N, Aranda R, Hargis L, et al. The KRAS(G12C) inhibitor MRTX849 reconditions the tumor immune microenvironment and sensitizes tumors to checkpoint inhibitor therapy. *Mol Cancer Ther* 2021;20:975–85.
48. Sharma P, Hu-Lieskovan S, Wargo JA, et al. Primary, Adaptive, and acquired resistance to cancer immunotherapy. *Cell* 2017;168:707–23.
49. Vander Velde R, Yoon N, Marusyk V, Durmaz A, Dhawan A, Miroshnychenko D, et al. Resistance to targeted therapies as a multifactorial, gradual adaptation to inhibitor specific selective pressures. *Nat Commun* 2020;11:2393.
50. Awad MM, Liu S, Rybkin II, Arbour KC, Dilly J, Zhu VW, et al. Acquired resistance to KRAS(G12C) inhibition in cancer. *N Engl J Med* 2021;384:2382–93.
51. Bear AS, Blanchard T, Cesare J, Ford MJ, Richman LP, Xu C, et al. Biochemical and functional characterization of mutant KRAS epitopes validates this oncoprotein for immunological targeting. *Nat Commun* 2021;12:4365.
52. Leidner R, Sanjuan Silva N, Huang H, Sprott D, Zheng C, Shih YP, et al. Neoantigen T-cell receptor gene therapy in pancreatic cancer. *N Engl J Med* 2022;386:2112–9.